Flow Around a Simplified Car, Part 2: Understanding the Flow

Siniša Krajnović
e-mail: sinisa@chalmers.se

Lars Davidson

Division of Fluid Dynamics,
Department of Applied Mechanics,
Chalmers University of Technology,
SE-41296 Gothenburg, Sweden

Results of a large eddy simulation (LES) are used to explore the flow around a generic car model. A new, refined picture of this flow is established. Many parts and aspects of this flow are studied and explained. The development of the instantaneous flow and its resulting time-averaged flow are depicted. Large differences are found between the instantaneous and the time-averaged flows. Special attention is given to the flow above the rear slanted surface. The origin, the development, and the interactions of the instantaneous vortices in this part of the flow are presented for the first time. This instantaneous flow is shown to be very unsteady and to contain a large number of different vortices that range in size from those of the size of the body over the intermediate hairpin-like vortices to very small coherent structures. Besides the variety in the length scales, the flow covers a wide spectrum of the time scales from the relatively steady motion of the cone-like trailing vortices on the slanted edges to highly frequent collisions of the hairpin-like vortices in the region of the attachment on the rear slanted surface.
[DOI: 10.1115/1.1989372]

Keywords: Large Eddy Simulation, LES, Generic Car, Vehicle Aerodynamics, Ground Vehicle

1 Introduction

Descriptions of flow features and their interactions are important for understanding the aerodynamic properties of a vehicle body. Probably the first picture of the flow around the ground vehicle body studied here (i.e., a body with a rear slant angle of 25°) was given by Ahmed et al. [1]. This included only a representation of the time-averaged flow around the rear part of the body. They observed two vortices trailing around the slanted side edges of the body. In addition to observing these vortices they found that the separation bubble in the near wake contains a pair of horseshoe vortices, situated one above the other. Ahmed et al. [1] also gave an explanation of the interactions of these structures on the basis of their measurements and visualizations and a rough description of the surface flow features on the rear slanted and vertical surfaces. The picture of the flow around the rear part of the body found in [1] was confirmed in the experimental work of Lienhart and Becker [2], who used more accurate measurements (laser-Doppler anemometry) than the measuring technique used in [1]. Another visualization study of the flow around this body is that of Spohn and Gillieron [3], who in addition to the wake flow also studied the flow along the body. The focus of their study was the instantaneous flow structures. The Reynolds number in their study was very low (8.3×10^3, based on the incoming velocity and the height of the body). To our knowledge the only description of the flow around the front part of the body of the Ahmed body at a Reynolds number comparable with that used in our large eddy simulation (LES) is that by Sims-Williams and Dominy [4]. They used oil-film visualization and registered three imprints of spanwise vortices (one on the top and one on each of the lateral sides of the body), similar to those found in Krajnović and Davidson [5] around the front of a similar body.

The present paper gives a thorough presentation of the flow structures and their interactions. The suggested vortical structures from [1,2,4] are compared with those found in our large eddy simulations. Their existence as well as the suggested explanation of their interactions are explored. The main objective of the present paper is to use the large amount of results from our LES calculations [6] together with state of the art visualization techniques to give an accurate representation of the flow. Both instantaneous and time-dependent structures are presented and the mechanisms of their origins are explained. The flow contains flow structures with a wide spectrum of time and length scales. These are studied with various visualization tools.

The paper is organized as follows: after the short review of visualization tools in Sec. 2, a brief summary of our LES calculation from [6] is given in Sec. 3.1. The flow around the front of the body is discussed in Sec. 3.2. This is followed by a description of the flow along the lateral edges of the body in Sec. 3.3. The most complex parts of the flow are those on the rear slanted surface and in the near wake, and these are described in Secs. 3.4 and 3.5, respectively. Finally, concluding remarks are given and the relevance and use of the results obtained are discussed in Sec. 4.

2 Visualization Tools

Several different visualization techniques were used to analyze the data from our LES calculations in [6]. Our experience is that different techniques are needed in different parts of the flow. The visualization software used in this paper is EnSight. The isosurfaces of the instantaneous second invariant of velocity gradient $Q=-1/2\partial u_i/\partial x_j \partial u_j/\partial x_i$ (see [7]) were used to study the temporal evolution of the coherent structures around the body. The time-averaged streamlines, velocity vectors, and isosurfaces of low static pressure were used to visualize time-averaged flow features. Vortex cores were calculated using EnSight postprocessing software which uses algorithms based on techniques outlined by Sujudi and Haimes [8]. Two of these algorithms are implemented in EnSight, the eigenvalue analysis algorithm and the vorticity-based algorithm. Both are linear and nodal, i.e., "*They are based on decomposing finite elements into tetrahedron and then solving closed-form equations to determine the velocity gradient tensor value at the nodes. Also, any variables with values at element centers are first averaged to element nodes before processing*" [9]. We have found in our previous work that the eigenvalue analysis algorithm is more suitable for the flows around ground vehicle bodies. "*This algorithm uses classification of eigenvalues and vectors to determine whether the vortex core intersects any faces of the decomposed tetrahedron*" [9]. Unfortunately, the eigenvalue analysis algorithm may produce false cores if the flow contains

Contributed by the Fluids Engineering Division for publication in the JOURNAL OF FLUIDS ENGINEERING. Manuscript received by the Fluids Engineering Division, July 26, 2004. Final revision: May 16, 2005. Associate Editor: Ismail B. Celik.

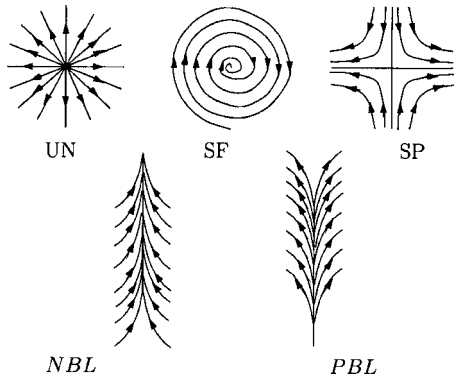

Fig. 1 Schematic representation of an unstable node (UN), stable focus (SF), and saddle point (SP). *NBL* and *PBL* are negative and positive bifurcation lines, respectively.

several vortices located close to each other [9]. In addition, both algorithms have difficulty finding the cores of curved vortices owing to the linear implementation of algorithms in EnSight [9]. As we will see later in the paper, this may cause problems in identifying the correct shape of the vortices in the near wake.

Time-averaged trace lines and streamlines are used to reveal critical points (i.e., points at which all the spatial derivatives of the velocity are zero) and bifurcation lines in the flow. Critical points can be classified into three main groups—nodes, foci, and saddles—of which nodes and foci can be stable and unstable (see Fig. 1). "*Bifurcation lines are lines drawn in the flow toward which the trajectories are asymptòtic*" [10]. They are denoted negative bifurcation lines (*NBL*) or positive bifurcation lines (*PBL*) depending on whether the trajectories on the wall are converging to or diverging from the bifurcation line (see Fig. 1). These lines are associated with flow attachment (*PBL*) or separation (*NBL*). For a complete description of critical points and bifurcation lines, we refer to [10].

3 Description of the Flow

3.1 Description of the LES Calculations. Large eddy simulations of the flow around the Ahmed body with the rear slanted surface at an angle of 25° (see Fig. 2) at a Reynolds number of about 2×10^5 (based on the height of the body and the velocity at the inlet) were reported in [6]. Three different computational grids were used and the present paper considers the results of the finest grid only. This computational grid contains around 16.5 million nodes which, in combination with a clever block arrangement, made possible a spatial resolution that has a resolution of $n^+<0.33$ in the wall normal direction, $13<\Delta s^+<250$ in the streamwise direction and $23<\Delta l^+<70$ in the direction parallel with the surface of the body and normal to the streamwise direction (the mean Δl^+ is around 30). Here $\Delta n^+=\Delta n\langle u_\tau\rangle_t/\nu$, $\Delta s^+=\Delta s\langle u_\tau\rangle_t/\nu$, $\Delta l^+=\Delta l\langle u_\tau\rangle_t/\nu$, and $\langle u_\tau\rangle_t$ is the time-averaged friction velocity. The time step was 1×10^4, giving a maximum CFL number of approximately 0.9 during the entire simulation. The averaging time, tU_∞/H, in the simulation was 38.2 (110,000 time steps). The time-averaged streamlines projected onto the several z planes downstream of the body were found to be approximately symmetric with respect to plane $y=0$, which indicates that the number of averaging samples and the averaging time were approximately sufficient. It should be mentioned that, in more careful investigation in the present paper, we found some asymmetry of the time-averaged flow with respect to plane $y=0$. This indicates that the flow contains some low-frequency events that require even longer averaging times. The computational time was already very long, however, and it was not possible to increase it considerably. The influence of the longer averaging time was tested (not shown here) on the medium grid simulation without finding any significant change in the flow features. As the flow structures are approximately the same on the medium and the fine grids in [6] we conclude that the averaging time of $tU_\infty/H=38.2$ is sufficient to produce an authentic picture of the mean flow. The subgrid-scale model used in the simulation was the standard Smagorinsky model with the constant $C_s=0.1$. A complete description of the numerical details in our LES calculations can be found in [6].

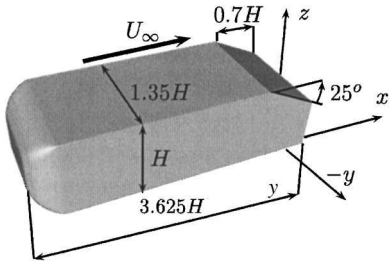

Fig. 2 Geometry of the Ahmed body. View from the side of the body. Note that *z*=0 is the ground plane and *x*=0 and *y*=0 are at the position of the rear vertical surface and the symmetry plane of the body, respectively.

This section describes the flow structures and their origins. Both the "real," i.e., the instantaneous flow, and the resulting time-averaged representation of that flow are considered. Observed flow features are compared with the findings of previous experimental studies. Some hypotheses presented in the past about the flow are closely examined and either confirmed or rejected on the basis of our findings. The presentation of the flow starts with the front part of the body, to continue with the flow along the body and its rear part. Finally the structures in the wake of the body are described.

3.2 Front Part of the Body. The flow around the front part of the Ahmed body is seldom studied, partly because of Ahmed et al.'s [1] stating that "*The interference between the rear end and the fore body flow is weak; this could be a consequence of the relatively long midsection.*" Two descriptions of the front part of the flow are given by Sims-Williams and Dominy [4] and Spohn and Gillieron [3]. The former discusses the flow at a Reynolds number of 1.71×10^5, based on the incoming velocity and the height of the body, which is close to that in the present paper. Sims-Williams and Dominy [4] used oil-film visualization to visualize the regions of the recirculating flows on the lateral sides and the roof of the body. Spohn and Gillieron [3] studied the instantaneous flow at a Reynolds number of 8.3×10^3 and found that the flow separates at the leading edge, forming vortical structures similar to Kelvin-Helmholtz vortices with their axes parallel to the separation line on the leading edge of the front of the body. Results of our LES calculations show that the instantaneous vortices are more of the hairpin-like type, similar to those found in [5], than of the Kelvin-Helmholtz type. They do not extend between the two foci found in the time-averaged flow (see Figs. 3 and 4) as assumed in the study by Spohn and Gillieron [3]. The identification of the Kelvin-Helmholtz vortices in [3] was based on two-dimensional photography from the lateral side of the body, which does not give sufficient information on the character of the vortical structures (i.e., two-dimensional, such as Kelvin-Helmholtz vortices, or three-dimensional, such as hairpin vortices). Thus the observation of the Kelvin-Helmholtz vortices in [3] probably has to do with the shortcomings of the visualization technique.

The oncoming time-averaged flow is divided on the front of the body into four regions, of which two end on the lateral sides, one on the top and one on the bottom side of the body (see Fig. 3). These regions are separated by positive bifurcation lines (such as PBL_f in Fig. 3) starting in the stagnation point and ending in the corners of the front surface. The flow separates as it reaches the

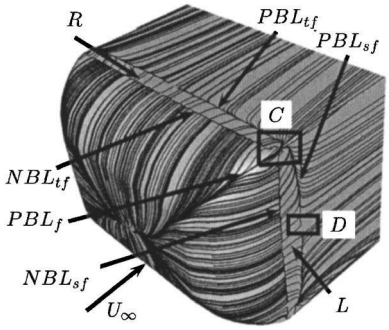

Fig. 3 Time-averaged trace lines on the surface of the body showing the roof and the lateral vortices. View of the front of the body from above and the lateral side.

top, the lateral, and the bottom sides of the body, forming negative bifurcation lines (NBL_{tf}, NBL_{sf}, and NBL_{lf}, respectively) as shown in Figs. 3 and 5. Figure 5 shows the underbody of the front of the vehicle. Downstream of these lines, we observe regions of recirculating flow (see *R* and *L* in Fig. 3 and *B* in Fig. 5). The imprints of vortices *R* and *L* in Fig. 3 are similar to those observed in [4]. The reattachments of the flows in regions *R*, *L*, and *B* are denoted by the positive bifurcation lines, PBL_{tf} and PBL_{sf} in Fig. 3, and PBL_{lf} in Fig. 5.

The flow following the positive bifurcation line, PBL_f (Fig. 3), splits into two parts (Fig. 4) that diverge and form two positive bifurcation lines (PBL_{tf} and PBL_{sf}), indicating the end of the separated flow (see Figs. 3 and 4). As this happens, the surface flow closest to the lateral edges moves in spiral motions ending in two stable foci, F_{ful} and F_{fsl} (see Fig. 4). These foci indicate the positions where vortices *R* and *L* are attached to the surface of the

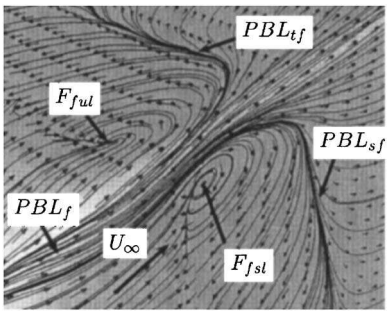

Fig. 4 Time-averaged trace lines on the surface of the body. Zoom of region *C* in Fig. 3 showing two foci, F_{ful} and F_{fsl}.

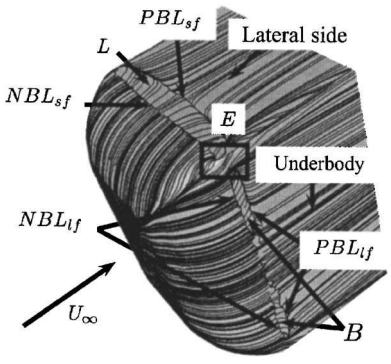

Fig. 5 Time-averaged trace lines on the surface of the body showing the vortices on the lateral side and underneath the body. View of the front of the body from below and the lateral side.

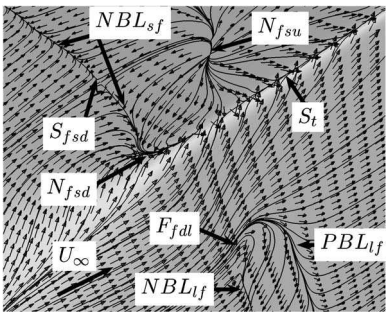

Fig. 6 Time-averaged trace lines on the surface of the body. Zoom of region *E* in Fig. 5 showing one stable N_{fsd} and one unstable node N_{fsu}, saddle point S_{fsd} and focus F_{fdl}.

body. The core of the time-averaged roof vortex, *R*, starts in focus F_{ful} and ends in the corresponding foci on the roof surface on the mirror side of the body (not shown here). Spohn and Gillieron [3] also identified two foci similar to F_{ful} and its mirror image.

The direction of the main part of the core of vortex *R* is parallel with the separation line, NBL_{tf} in Fig. 3. In the same way, the lateral vortex, *L*, in Fig. 3 is parallel with its separation line. The vortex core starts in focus F_{fsl} (in Fig. 4) and stretches parallel with the line of separation indicated by the NBL_{sf} (see Fig. 3). The lower corner of the front of the body is shown in Fig. 6. The instantaneous vortices downstream of this corner and along the edge S_t are presented in Fig. 7. Two different kinds of instantaneous vortices are shown in this figure, λ and T_i vortices. The λ vortex shown in Fig. 7 is a so-called hairpin vortex and is formed in the following way: as the instantaneous flow separates at the lateral rounded edge of the body approximately at the position of the NBL_{sf} in Fig. 3, vortices are formed parallel with the instantaneous separation line (which is approximately at the position of time-averaged separation line NBL_{sf}). On their way downstream, their middle parts are lifted from the surface of the body, forming hairpin vortices, λ. When averaged, the λ vortices form the time-averaged lateral vortex *L* (we can see the imprint of *L* on the body in Fig. 3). Similar hairpin vortices are formed in the instantaneous flow on the roof of the body, approximately downstream of the NBL_{tf}. These structures average into the time-averaged vortex *R* in Fig. 3. The merging of the instantaneous structures λ and T_i in region *M* is visualized in Fig. 7.

At approximately half the body height, positive bifurcation line PBL_{sf} is divided by saddle point S_{fsl} (see Fig. 8). At approximately the same height, there is a saddle point on NBL_{sf} (not shown here). In a similar way, the flow coming from the opposite sides of lines PBL_{tf} and NBL_{tf} (see Fig. 3) on the roof of the body

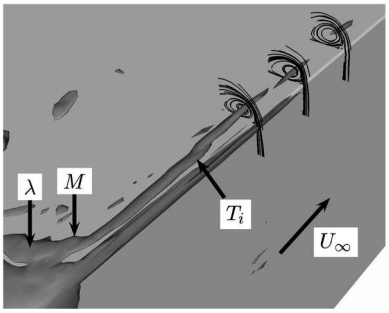

Fig. 7 The isosurface of the instantaneous second invariant of the velocity gradient, Q=4000, around the lower lateral edge. T_i are the instantaneous structures that average to become the time-averaged vortex in Fig. 9. *M* indicates the approximate position of merging of λ vortices on the lateral side with the T_i structures. View of the body from below and the lateral side.

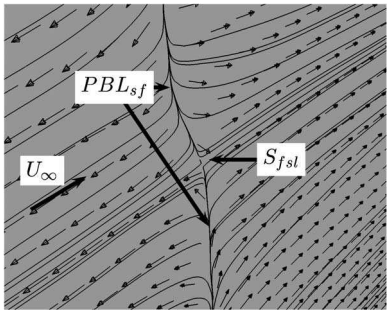

Fig. 8 Time-averaged trace lines on the surface of the body. Zoom of region *D* in Fig. 3 showing saddle point S_{fsl}.

collides in saddle points (not shown here).

The lower side of the body displays the separated region *B* which is divided into three parts (see Fig. 5). We have found that both the negative bifurcation line, NBL_{lf} (separation), and the positive bifurcation line, PBL_{lf} (reattachment), stretch only one-third of the width from each lateral edge (see Fig. 5). It was difficult to identify the bifurcation lines in the middle one-third of the width of the body. As seen in [6], separation region *B* is much thinner than regions *R* and *L* on the roof and the lateral sides, respectively.

We shall now consider the flow around one of the lower front corners (*E* in Fig. 5) shown in Fig. 6. The time-averaged separation region on the lateral side extends from the upper to the lower corners of the lateral side in Fig. 3. (all the way from focus F_{fsl} in Fig. 4 to the stable node N_{fsd} in Fig. 6). One saddle point, S_{fsd} (Fig. 6), was found on the NBL_{sf} close to node N_{fsd}. The unstable node, N_{fsu}, appears as we move downstream on the lateral side of the body. Figure 6 indicates that the surface flow is redistributed in N_{fsu} in all four directions in a spiral shape.

Let us now return to the flow close to the leading edge of the bottom side of the body (see Figs. 5 and 6). As mentioned earlier the flow separates on the bottom edge. The upstream flow that reaches the bottom side of the body closest to the lateral edge is deflected toward that edge and feeds the longitudinal trailing vortex stretching along edge S_t (see Fig. 6). The rest of the surface flow is attached on the surface for approximately one-tenth of the width and separates close to stable focus F_{fdl} (see Fig. 6). This point indicates the singular point between the negative and positive bifurcation lines, NBL_{lf} and PBL_{lf}. We have found that the origin of the vortex core of time-averaged vortex *B* is located in this point (not shown here). The vortex core of *B* was difficult to identify in the middle one-third of the width of the body.

Krajnović and Davidson [5,11] studied the flow around a similar body and observed no separation at the leading lower edge. A possible explanation of the change from attached flow in [5,11] to separated flow in the present study is that the ground clearance, $c/H=0.17$, in the present flow is larger than $c/H=0.08$ in [5,11]. The larger ground clearance allows the flow to separate and then reattach, forming coherent structures. Another possible explanation is related to the spatial resolution used in [5,11]. We found that the separating bubble *B* is very thin and was observed only in the fine mesh LES [6]. Thus it is possible that a similar bubble exists in the flow in [5,11] but was not detected owing to relatively insufficient resolution.

3.3 Longitudinal Vortices Along the Body. Boundary layers are formed both on the stationary floor and the underbody of the car model. These decelerate the fluid and, to satisfy continuity, the fluid, instead of accelerating in the center region between the floor and the underbody, spreads outward to the lateral sides and forms the coherent structures, T_i, in Fig. 7 that average into the longitudinal vortex in Fig. 9.

This time-averaged longitudinal vortex initially grows in diameter along the lateral edge, S_t, in the downstream direction. Then, downstream of approximately $x=-1.5H$, it has a constant diameter for the main part of the body length (see Fig. 9). The core of the vortex in Fig. 9 keeps the initial position in the *x-y* plane along and behind the body. Some longitudinal structures (*LS*) were observed above the floor [see Fig. 9(*b*)]. It is not clear whether these were caused by the stationary floor or whether they are a result of insufficient averaging time.

3.4 Rear Slanted Surface of the Body. This section describes the part of the flow that has the greatest influence on the aerodynamics of the body, i.e., the flow on the slanted surface. The instantaneous flow structures are described first. This is followed by a presentation of the picture of the resulting time-averaged flow.

3.4.1 Instantaneous Flow on the Rear Slanted Surface. The fluid separates at the sharp edge [S_s in Fig. 10(*a*)] between the roof surface and the slanted rear surface. Elongated coherent structures that extend in the spanwise direction are formed as a result of this separation. The axes of these structures are parallel with the edge along the middle part of the edge. The vortices that

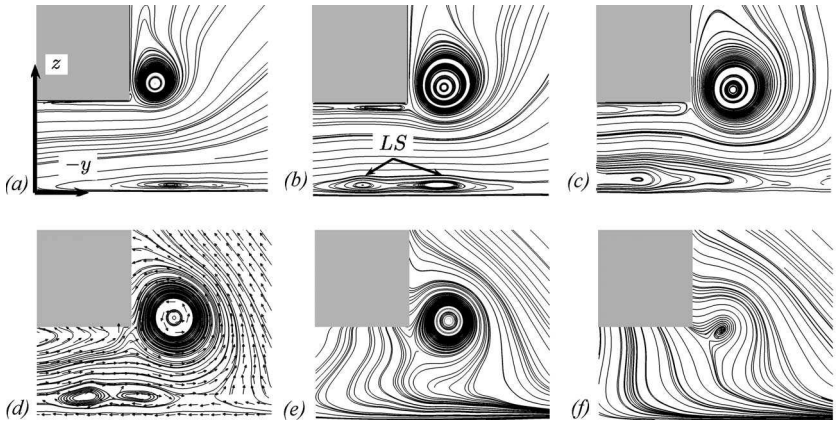

Fig. 9 Time-averaged streamline projected onto planes: (*a*) $x=-2.08H$, (*b*) $x=-1.39H$, (*c*) $x=-0.69H$, (*d*) $x=0$ (the plane of the rear vertical surface), (*e*) $x=0.21H$, and (*f*) $x=0.38H$. View from the front of the lower left edge of the body. Note that *z* and *y* axes in the figure do not indicate the origin of the coordinate system. The real $y=0$ is at the position of the symmetry plane of the body. Flow is from the observer into the plane.

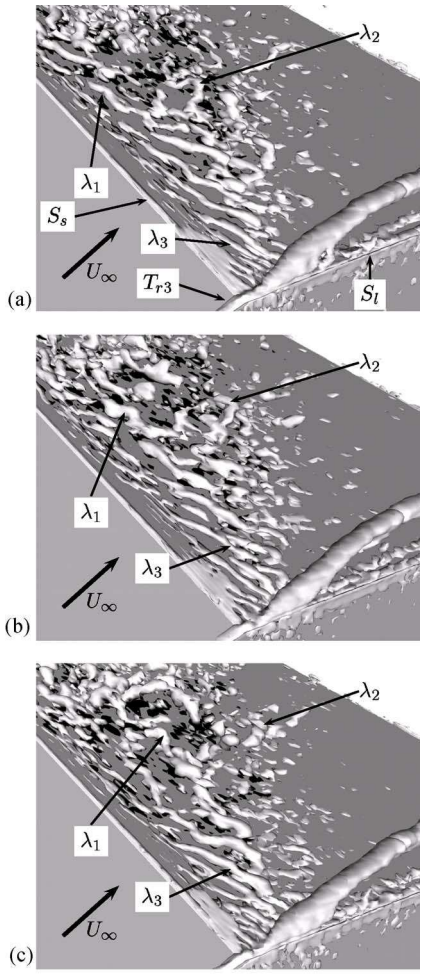

Fig. 10 The isosurface of the instantaneous second invariant of the velocity gradient, $Q=6500$. The time difference between two pictures is $tU_\infty/H=0.055$. Flow is from left to right and the view is from the lateral side and above the body. The sharp edge between the roof and the slanted surface is denoted by S_s and the slanted lateral edge is denoted by S_l. Vortices are colored by the streamwise velocity. The white vortices are traveling downstream and the black vortices are traveling upstream.

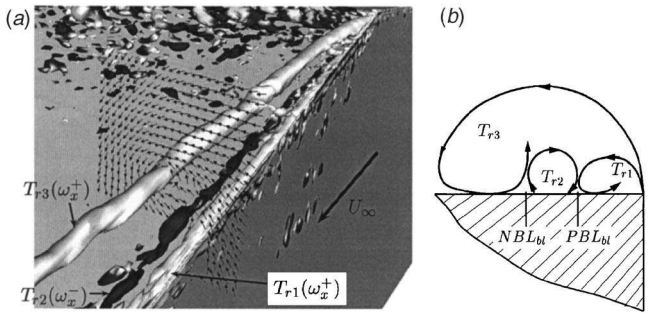

Fig. 11 (*a*) The isosurface of the instantaneous second invariant of the velocity gradient, $Q=6500$. View is from behind and the lateral side of the right slanted edge. Note that only core parts of the cone vortices are shown. The cone vortices are colored by the vorticity component in the streamwise direction ω_x. Vortices colored with black and white have clockwise and counter-clockwise directions of rotation, respectively. (*b*) Schematic representation of the mantles of vortices T_{r1}, T_{r2}, and T_{r3} seen from behind the body. The positions of NBL_{bl} and PBL_{bl} near the opposite lateral side are also shown in Fig. 16(*b*).

are born close to the end of the edge are tilted so that they travel toward the center of the slanted surface. When the spanwise vortices are convected downstream, they merge with each other to form slightly larger vortices such as λ_1 in Fig. 10(*a*). The next step in their development is further merging and becoming larger, such as λ_1 in Fig. 10(*b*), before their tip is lifted from the surface and forms hairpin-like vortices [see λ_1 in Fig. 10(*c*)]. Their life as hairpin vortices with both legs attached on the slanted surface [such as λ_2 in Fig. 10(*a*)] is short. One of their legs separates from the surface or is simply broken, such as in λ_2 in Fig. 10(*b*). Finally, close to the reattachment around the half length of the slanted surface, the other leg of the vortex is destroyed [see λ_2 in Fig. 10(*c*)] and only a small part continues downstream and possibly enters the wake region. Vortices traveling downstream are colored white and those traveling upstream are colored black. As we can see, the recirculation region contains chiefly vortices that travel downstream (see Fig. 10). They are much stronger than the black-colored vortices close to the surface, which are traveling upstream.

The flow coming from the lateral side up over the slanted lateral edge [S_l in Fig. 10(*a*)] at high velocity separates, which results in a pressure suction peak along the edge. This takes place on two levels. One thin cone-like vortex, T_{r1}, is formed close to the slanted edge with a larger vortex, T_{r3}, around it (see Fig. 11). These vortices are reminiscent of a gearwheel mechanism although they do not actually drive each other. The rotational movement of the mantle of vortex T_{r3} (gearwheel number three) starts as the shear layer on the slanted edge, S_l, follows the conical path, and ends on the slanted surface [see Fig. 11(*b*)]. When the mantle again leaves the surface to continue counter-clockwise rotation, it draws the neighboring fluid particles in the upward direction [see the sketch in Fig. 11(*b*)]. On the other side of vortex T_{r2}, vortex T_{r1} (gearwheel number one) reattaches on the slanted surface, drawing its neighboring fluid particles down toward the surface. These two mechanisms produce the third cone-like vortex, T_{r2} (gearwheel number two), with a clockwise direction of rotation (see Fig. 11). Only two of these vortices (i.e., T_{r2} and T_{r3}) were observed in previous studies by Ahmed et al. [1] and Spohn and Gilleron [3].

The motion of the fluid from the lateral side to the slanted surface that is involved in the formation of "gearwheel" vortices can be observed upstream of the separation edge, S_s (see vortex T_{r3} in Fig. 10). One of these time-averaged vortices is shown in Fig. 12. We found that these vortices stretch upstream to approximately $x=-1.56H$. A similar motion of fluid from the lateral side to the roof (over the upper lateral edge) was observed in the instantaneous flow in [3] at position $x=-0.768H$. Note that $x=0$ and $z=0$ are the positions of the rear vertical surface of the body and

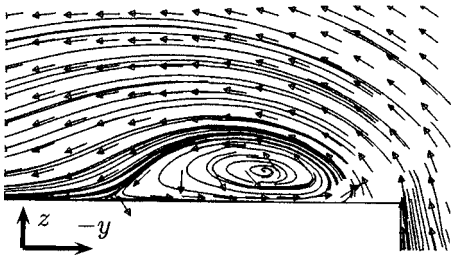

Fig. 12 Time-averaged streamlines and velocity vectors projected onto plane $x=-0.8H$. View from the front of the upper left lateral edge. Flow is from the observer into the plane. Note that $z=0$ is the ground plane and that the z and y axes in the figure do not indicate the origin of the coordinate system. The real $x=0$ and $y=0$ are at the position of the rear vertical surface and the symmetry plane of the body, respectively.

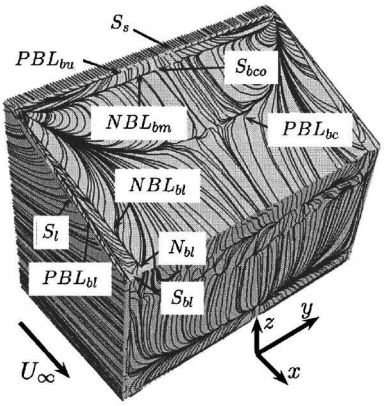

Fig. 13 Time-averaged trace lines on the rear slanted surface of the body. View of the lateral, slanted, and rear vertical faces of the body.

the ground of the wind tunnel, respectively.

Let us now return to the spanwise vortices close to the upper corners of the slanted surface (such as λ_3 in Fig. 10). As already mentioned, their axes are tilted with respect to edge S_s. This behavior is caused by the cone-like shape of vortex T_{r3}. As it propagates downstream, it grows in diameter, pushing the λ vortices away from the slanted edge, S_l. The resulting orientation of the λ vortices closest to the T_{r3} is toward the center of the slanted surface.

3.4.2 Time-Averaged Flow on the Rear Slanted Surface. Engineers' interest is often limited to time-averaged quantities such as mean lift and drag forces, which consist mainly of the pressure contributions from the rear of the body. Besides the indication of the low pressure regions on the surface of the body, the time-averaged structure tell us about the vortex-induced mean aerodynamic forces. One good example is cone-like vortices on the rear window of some cars that cause vortex-induced drag and lift. (As we will see later in the text such vortices are formed on the slanted surface of the vehicle studied in this paper.) Other issues, such as regions of accumulation of dirt and water, can also be addressed studying the time-averaged picture of the flow. These are only some examples of where knowledge of the time-averaged flow is helpful in the vehicle design process.

In the following sections we present the time-averaged flow around the rear of the body, keeping in mind that the real flow is very time dependent and that the time-averaged picture only gives *a measure* of the flow that is interesting in terms of design.

When the instantaneous structures on the slanted surface described above are averaged, they form the flow structures that are indicated by surface patterns shown in Fig. 13. We describe these structures in the following text and explain their meaning.

The largest imprint on the slanted surface stretches from edge S_s and the positive bifurcation line, PBL_{bc} (see Fig. 13). A more detailed picture of the fluid motion on the surface in the region between edge S_s and PBL_{bc} can be seen in Fig. 14. The fluid separates along NBL_{bm} and reattach at the position of PBL_{bu} [see Figs. 14(*a*) and 14(*b*)]. From PBL_{bu} the fluid particles move downstream toward the NBL_{bm} and upstream toward edge S_s [see Figs. 14(*a*) and 14(*b*)]. On both sides of PBL_{bu}, the flow direction is parallel with the x axes close to the center plane, $y=0$ [see Figs. 14(*a*) and 14(*b*)], and changes its direction to a more spanwise one [i.e., in the y direction] away from the center plane [see the left side of Fig. 14(*a*)]. The mirror symmetry of the flow around plane $y=0$ on the NBL_{bm} results in one critical point in the saddle point, S_{bco}, in Fig. 14(*b*). Downstream of the NBL_{bm} the flow moves from the PBL_{bc} in Figs. 13 and 14(*c*). The two parts of the PBL_{bc} meet in the very unsteady flow region in Fig. 14(*c*). We expected

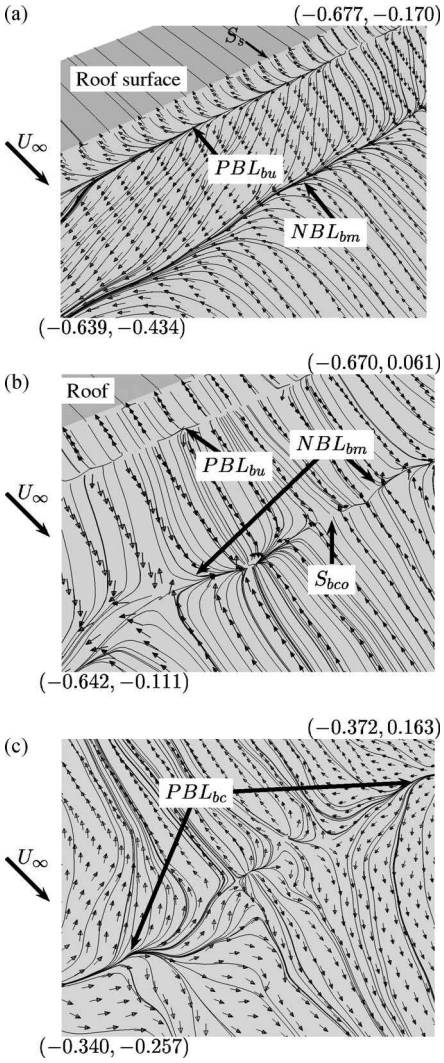

Fig. 14 Time-averaged trace lines on the surface of the body. (*a*) Zoom of the patterns in Fig. 13 showing NBL_{bu} and NBL_{bm}. (*b*) Zoom of the patterns in Fig. 13 showing saddle point S_{bco}. (*c*) Zoom of the unsteady reattachment in Fig. 13. Coordinates ($x/H, y/H$) are given for lower left and upper right corners in all three figures. The lateral sides are located at $y=\pm 0.675H$.

a saddle point here similar to those on the front part of the body (for example S_{fsl} in Fig. 8). No critical point was found here because the flow has not fully converged owing to very unsteady flow around the reattachment [see Fig. 14(*c*)], although we averaged over a very long time period (110,000 time steps corresponding to time $tU_\infty/H=38.2$). This highly unsteady separation can also be observed in the oil-film visualization in [2] and in the visualization of the instantaneous flow in [3]. Spohn and Gillieron [3] suggested that the unsteadiness in this flow region is caused by oscillations of the trailing vortices themselves and their interactions with vortices shed from the front. We found the trailing vortices to be relatively steady, with their cores remaining at approximately the same position for a long period of time. It is more likely that the interaction between λ vortices is the reason for the high levels of unsteadiness at the lower part of the slanted surface. As the λ vortices traveling in the streamwise direction (such as λ_1 and λ_2 in Fig. 10) approach the region of the reattachment, they break up (as described above) and meet the λ vortices coming from the upstream corners (such as λ_3 in Fig. 10). These meetings result in a large number of collisions which together with the break-up of vortices such as λ_1 and λ_2 make this region of the

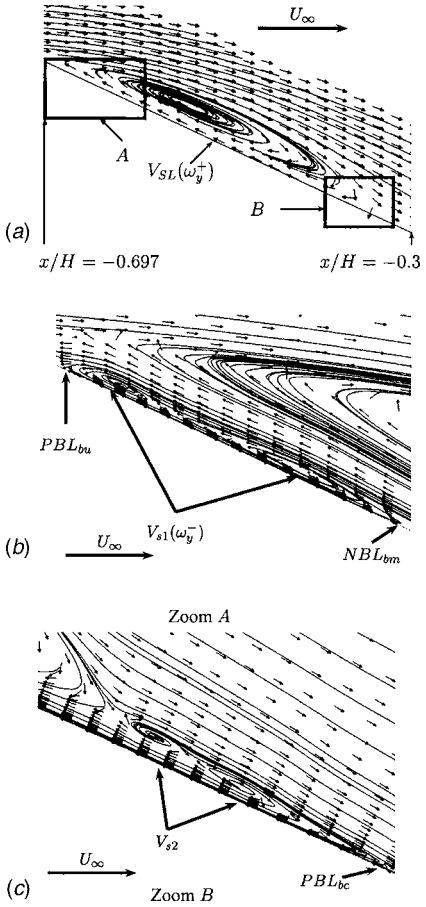

Fig. 15 (*a*) Time-averaged streamlines and velocity vectors projected onto symmetry plane *y*=0 showing the flow above the slanted surface. The velocity vectors are extrapolated and plotted on coarser grid than that used in the simulation to make the direction of the flow visible. (*b*) Zoom *A* from (*a*). (*c*) Zoom *B* from (*a*). The direction of rotation of vortices is indicated by the vorticity component in the *y* direction (i.e., ω_y^+ and ω_y^- are positive and negative vorticity components, respectively).

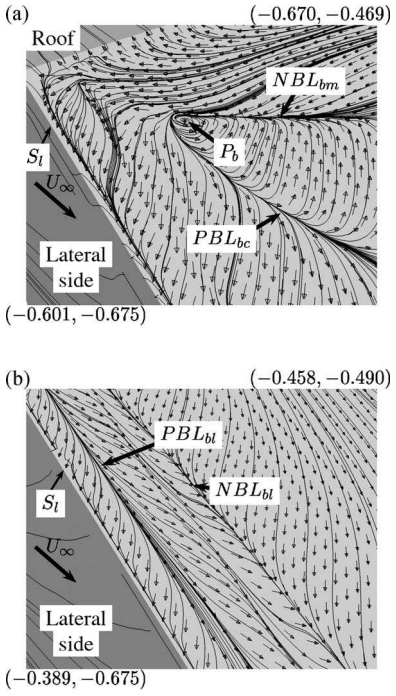

Fig. 16 Time-averaged trace lines on the surface of the body. (*a*) Zoom of the patterns in Fig. 13 showing the stable focus, P_b. (*b*) Zoom of the patterns in Fig. 13 showing the negative and positive bifurcation lines, NBL_{bl} and PBL_{bl}, respectively. Coordinates ($x/H, y/H$) are given for lower left and upper right corners in both figures. NBL_{bl} and PBL_{bl} are also shown in Fig. 11(*b*).

flow very unsteady. Thus we believe that the unsteady character of the flow in the lower part of the slant is not a direct consequence of the trailing vortices. It is rather the result of their indirect influence on the λ_3 vortices, making them change their paths (as previously mentioned) and interacting with the λ_1 and λ_2 vortices.

The information from Fig. 14 is not sufficient to allow conclusions to be drawn about the time-averaged structures above the slanted surface. The imprints of the vortices in Fig. 14 could for example be interpreted as the traces of one vortex between edge S_s and the PBL_{bu} (rotating with positive vorticity ω_y^+), one vortex between the NBL_{bm} and the PBL_{bu} (rotating with negative vorticity ω_y^-) and one vortex between the NBL_{bm} and the unsteady region of PBL_{bc} in Fig. 14(*c*) (rotating with positive vorticity ω_y^+). Let us now consider the flow picture in the symmetry plane, $y=0$, in Fig. 15. We see that the main part of this region is dominated by the large vortex V_{SL} in Fig. 15(*a*), which has a positive direction of rotation ω_y^+ and stretches between spanwise edge S_s and some position upstream of the unsteady region in the middle of PBL_{bc} [see Fig. 15(*a*)]. In the upper part of the slant [see Fig. 15(*b*)], we find vortex V_{s1}, which rotates in the negative direction (ω_y^-) and is located below vortex V_{SL} and between PBL_{bu} and NBL_{bm}. It was found that this vortex extends at least out to $y=\pm 0.625H$ in the spanwise direction. It is worth mentioning that the flow is very unsteady at the position of V_{s1} and a very long time is required to average it. The unsteady flow just above the unsteady reattachment in PBL_{bc} appears to form the vortex structure V_{s2} [see Fig. 15(*c*)]. This is not a real vortex but a result of highly unsteady flow in this region and disappears as we move from the symmetry plane toward lateral edge S_l. Similar unsteady reattachment was observed in the experiments by Lienhart and Becker [2].

The positive and negative bifurcation lines, PBL_{bc} and NBL_{bm}, meet close to the slanted edge, S_l [see Fig. 16(*a*)]. The direction of the fluid around these lines results in a critical point in the form of a stable focus, P_b. Such a focus was also found in the experiments of Spohn and Gillieron [3]. This focus is the origin of the vortex core of vortex V_{SL} [see Fig. 15(*a*)] that stretches to the mirror focus on the other side of plane $y=0$.

3.4.3 Time-Averaged Cone-like Trailing Vortices. Figure 16(*b*) shows the existence of the negative bifurcation line, NBL_{bl}, and the positive bifurcation line, PBL_{bl}, close to the slanted edge, S_l. Instantaneous vortices T_{r1}, T_{r2}, and T_{r3} (see Fig. 11) average to three time-averaged vortices that are located around these bifurcation lines. Figure 17 shows these vortices above the imprints in Fig. 16 (thus the mirror side of that shown in Fig. 11). The mechanism of feeding the chief trailing vortex, T_{3l}, with the upstream flow is illustrated in Fig. 17(*a*). The streamlines, STR_l, that come parallel with the streamwise direction of the flow are first deflected upward toward the lateral slanted edge, S_l, and then sucked in above the slanted surface. Further downstream they continue to roll around the vortex core of vortex T_{3l} [see Fig. 17(*a*)]. The upward deflection of the lateral flow toward the lateral slanted edge can also be observed in Fig. 13 (here in the pattern of the trace lines on the surface of the lateral side of the body that are deflected toward the slanted edge, S_l). Similar to the instantaneous vortices, the time-averaged ones have direction of rotation similar to three gearwheels placed in tandem [see Fig. 17(*b*)].

The process of formation of vortex V_{SL} can be followed in Fig.

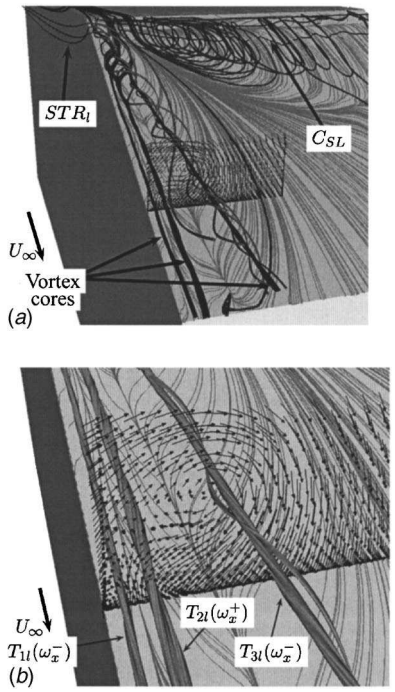

Fig. 17 (*a*) Vortex cores of the time-averaged vortices wrapped in the streamlines that are generated using vortex cores as a source. Time-averaged trace lines are shown on the surface. View from behind the body. (*b*) Zoom of (*a*). (Note that streamlines STR_l are removed in this zoom for clarity.)

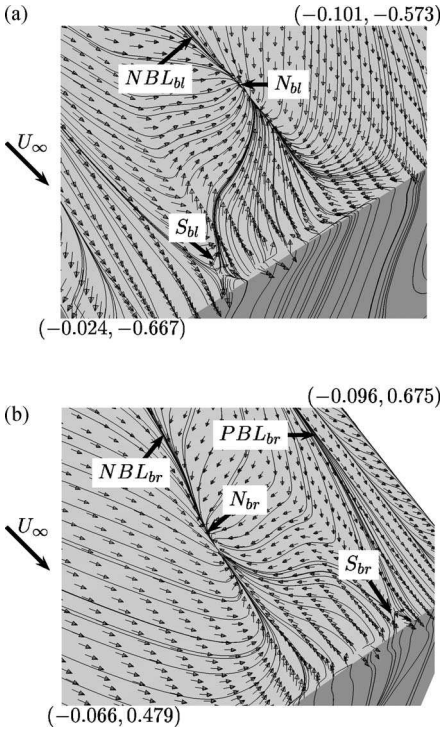

Fig. 18 Time-averaged trace lines on the surface of the body. Zoom of the flow structures from Fig. 13 showing (*a*) the lower left corner of the slanted surface and (*b*) the lower right corner of the slanted surface. Coordinates (*x*/*H*, *y*/*H*) are given for lower left and upper right corners in both figures.

17(*a*). The streamlines coming from above the roof of the body are pulled in toward the low pressure recirculating region rolling in spiral motion around vortex core C_{SL} [see Fig. 17(*a*)].

Let us now consider the flow close to the downstream corners of the slanted surface shown in Fig. 18. Two stable nodes, N_{bl} and N_{br}, are formed close to the lower corners of the slanted surface (see Fig. 18). Located on the negative bifurcation lines, NBL_{bl} and NBL_{br}, these nodes attract most of the surface flow that is located under vortices T_{2l}, T_{2r} and T_{3l}, T_{3r} (see Fig. 17). The flow between vortices T_{1l}, T_{1r} and T_{2l}, T_{2r} splits in saddle points S_{bl} and S_{br}. Although the instantaneous flow in the region between S_{bl} (S_{br}) and N_{bl} (N_{br}) changes direction between downstream and upstream, the upstream motion prevails (see the time-averaged flow in Fig. 18).

3.5 Near-Wake Flow. The previous work of Ahmed et al. [1] suggested that the near-wake flow contains two horseshoe vortices situated one above the other with their legs stretching in the streamwise direction. This section presents the survey of this flow region from our LES results. The assumptions of Ahmed et al. [1] about the flow structures in the near wake will be investigated and a new, revised picture of this flow will be established.

We have used two visualization techniques to investigate this part of the flow. The first technique uses vortex cores and projections of the streamlines on planes across the wake in all three directions. Five such planes are shown in Fig. 19(*a*). Planes $y=0$ and $y=0.521H$ in this figure show the existence of two vortices, U_h and U_l, one above the other. As we move toward the lateral side (from $y=0$ to $y=0.521H$), the core of the upper vortex, U_h, moves in the positive z direction [see vortex core in Fig. 19(*a*)]. The legs of U_h are bent in the streamwise direction at approximately $y=\pm 0.53H$ and stretch in the streamwise direction [see planes $x=0.347H$, $x=0.868H$ and $x=1.389H$ in Fig. 19(*a*)]. The core of the lower vortex, U_l, keeps approximately the same height with respect to the floor (approximately $z=0.07H$). It bends at $y=\pm 0.6H$ and two legs are formed that extend in the positive z-direction. Figure 19(*a*) shows that cone-like vortex T_{3l} and the upper vortex, U_h, both move downstream in the near wake but that the lower vortex, U_l, does not (see planes $x=0.347H$, $0.868H$, and $x=1.389H$). However, we have found that this vortex moves in the positive z direction (not shown in this figure). Moving in the positive z direction, the focus of vortex U_l moves toward the body.

The technique of low pressure isosurfaces and the vortex cores is used in Fig. 19(*b*) to visualize the time-averaged vortices around the rear part of the body. From the description of horseshoe vortices U_h and U_l found above, it is clear that they are very curved between their tips and legs. As mentioned in Sec. 2, the algorithm used for the calculation of vortex cores has a linear implementation and thus has difficulty finding the cores of curved vortices. This is probably the reason why both cores of the curvatures between the tip and legs of vortex U_h and one (the left one) of vortex U_l are missing in Fig. 19(*b*). We also mentioned in Sec. 2 that the eigenvalue analysis algorithm may produce incorrect results when the flow contains several vortices close to each other. Here we have two vortices of approximately the same strength, and their cores appear to merge into one ring-like vortex core in Fig. 19(*b*). Although these two vortices interact with each other, as we have seen above, they exist as two separate vortices. Another explanation of the discontinuous vortex cores and slightly false picture of the vortex cores in Fig. 19(*b*) can be that the flow has not completely converged in time.

Ahmed et al. [1] studied these structures and concluded, in agreement with our observations, that the vortex tips of U_h and U_l are approximately parallel with the base surface of the body. They found the streamwise extension of the legs of vortex U_h and concluded that these merge with the trailing cone-like vortices T_{3l} and T_{3r}. Our results confirm their findings [see Fig. 19(*a*)]. As vortex T_{3l} weakens in strength and appears to vanish downstream of position $x=0.57H$, the U_h vortex continues its extension after that

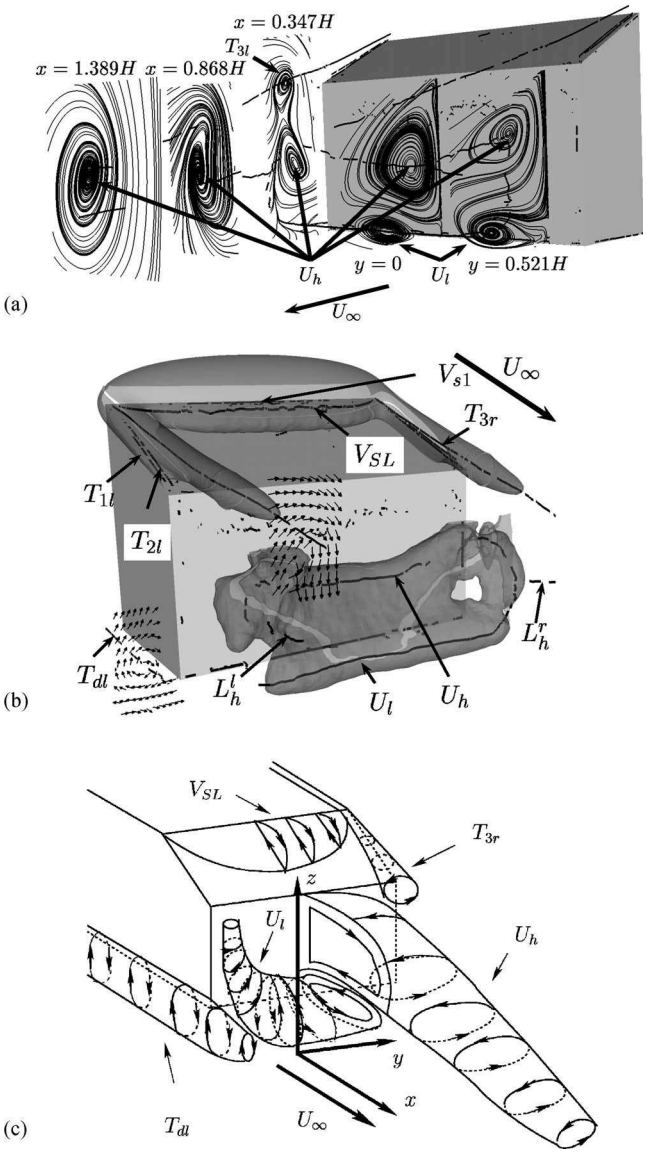

Fig. 19 Time-averaged near-wake flow. (*a*) Time-averaged streamlines projected onto planes (from left to right in the figure): $x=1.389H$ ($-0.675H \leq y \leq 0$, $0.174H \leq z \leq 0.833H$), $x=0.868H$ ($-0.675H \leq y \leq -0.278H$, $0.174H \leq z \leq 0.833H$), $x=0.347H$ ($-0.675H \leq y \leq -0.382H$, $0.174H \leq y \leq 1.042H$), $y=0$ ($-0.59H \leq x \leq 0$, $0.174H \leq z \leq 0.833H$) and $y=0.521H$ ($-0.59H \leq x \leq 0$, $0.174H \leq z \leq 0.833H$). (*b*) Isosurfaces of the static pressure, $p=-0.16$ and $p=-0.19$. L_h^l and L_h^r are cores of the legs of vortex U_h. (*b*) Schematic representation of the time-averaged wake flow. Note that only half of the horseshoe vortices U_l and U_h for $y \leq 0$ and $y \geq 0$, respectively, are shown.

position and grows in diameter. Cone-like vortices T_{3l} and T_{3r} probably enter the horseshoe vortex, U_h, somewhere downstream of $x=0.57H$.

A schematic representation of the time-averaged flow structures shown in Fig. 19(*c*) summarizes the vortices around the rear of the body. Only half of the U_h and U_l vortices in the positive and negative y directions, respectively, are shown in this figure for the sake of clarity. As shown in this sketch, the downstream extension of the U_l vortex assumed in the work of Ahmed et al. [1] is probably incorrect and it is here revised with a somewhat odd extension of this vortex in the positive z-direction. It is possible that vortex U_l interacts with the longitudinal vortices T_{dl} and T_{dr}. However, already along the body the vortices T_{dl} and T_{dr} are weak compared to the cone-like vortices T_{3l} and T_{3r}. Their strength downstream the body is even smaller (see Fig. 9) and their influence on the vortex U_l is probably negligible (note that the size of the vortices and in particular of T_{dl} in Fig. 19 are not drawn to scale).

4 Conclusions and Relevance of the Results

Results of large eddy simulations in conjunction with visualization tools are used to establish complete pictures of both the instantaneous and the time-averaged flows around an Ahmed body with a rear slant angle of 25°. The flow contains a large variety of time and length scales that interact with each other, making the flow extremely complex. Among the instantaneous coherent structures found in the flow, two structures distinguish themselves, cone-like vortices along the rear slanted edges and hairpin-like vortices in the regions of separated flows on the front and the rear slanted surface of the body. Both the time and the length scales of these two structures differ. While the cone-like vortices are of the size of the body and are relatively steady, the hairpin-like vortices are very small structures that change in shape over a short period of time.

Our detailed study has not only presented the unknown instantaneous flow around the Ahmed body but also enriched our knowledge of the time-averaged flow. For example, it has been found that the flow on the rear slanted surface contains three pairs of cone-like vortices as compared to only two pairs known from previous experimental studies. The inaccurate position of the horseshoe vortices, assumed in the experiments of Ahmed et al. [1] to be located one above the other in the wake with their legs stretching in the streamwise direction, was corrected here. Flow around the front of the body is presented for the first time, showing rich flow patterns on all four sides of the body.

Although a very detailed picture of the flow is presented in this paper, it is important to reflect on the relevance of the information provided here. Information on flows around ground vehicle bodies has previously been limited to the time-averaged flow (such as in [1]). We have tried in this paper to provide both the instantaneous and time-averaged representation of the flow. It has been difficult to find some sense and structure in some parts of the instantaneous flow, and more results from the time-averaged flow are reported in the present paper. The time-averaged flow structures are more smooth than the instantaneous ones and are easier to analyze. We are used to seeing time-averaged structures in textbooks and can relatively easily identify them. Previous knowledge about instantaneous flow structures around the body studied in the present work was very poor and was gathered from only a few experimental studies that chiefly present flow visualizations at low Reynolds numbers. The present paper gives a description of a large part of this instantaneous flow.

Much of the influences on the aerodynamics of the vehicle, such as directional stability and wind noise, can only be understood if the instantaneous flow can be accurately represented. If the real flow is very time dependent and is never coincident with the time-averaged flow, what is the meaning of the time-averaged flow? The time-averaged vortices on the surface of the body tell us about the parts of the body that are affected by large pressure forces that cause aerodynamic forces and moments. The time-averaged streamlines on the surface expose the regions where water and dirt accumulate over a long period of time. The time-averaged coherent structures around the body give an explanation of the vortex-induced mean drag and lift forces. However, if we want to study the processes of vortex interaction that cause the change in aerodynamic forces, for example, we must study the instantaneous flow.

Some parts of the time-averaged flow studied in the present paper, such as flow above the slanted surface (apart from the cone-like vortices), are completely different from their instantaneous counterparts. Another example is the time-averaged wake flow containing horseshoe vortices U_h and U_l, where the corre-

sponding instantaneous flow contains only smaller irregular structures that change over time. The relevance of the time-averaged flow in such regions for the aerodynamic properties of the vehicle is probably very small.

Acknowledgments

This work was supported by the FLOMANIA project. The FLOMANIA (Flow Physics Modelling-An Integrated Approach) is a collaboration between Alenia, AEA, Bombardier, Dassault, EADS-CASA, EADS-Military Aircraft, EDF, NUMECA, DLR, FOI, IMFT, ONERA, Chalmers University, Imperial College, TU Berlin, UMIST, and St. Petersburg State University. The project is funded by the European Union and administrated by the CEC, Research Directorate-General, Growth Programme, under Contract No. G4RD-CT2001-00613. Computer time on the Linux cluster, provided by the NSC (National Supercomputer Center in Sweden), is gratefully acknowledged.

References

[1] Ahmed, S. R., Ramm, G., and Faltin, G., 1984, "Some Salient Features of the Time Averaged Ground Vehicle Wake," SAE paper no. 840300.

[2] Lienhart, H., and Becker, S., 2003, "Flow and Turbulent Structure in the Wake of a Simplified Car Model," SAE paper no. 2003-01-0656.

[3] Spohn, A., and Gillieron, P., 2002, "Flow Separations Generated by a Simplified Geometry of an Automotive Vehicle," in *IUTAM Symposium: Unsteady Separated Flows*, April 8–12, Toulouse, France.

[4] Sims-Williams, D. B., and Dominy, R. G., 1998, "Experimental Investigation Into Unsteadiniess and Instability in Passanger Car Aerodynamics," SAE paper no. 980391.

[5] Krajnović, S., and Davidson, L., 2003, "Numerical Study of the Flow Around the Bus-Shaped Body," ASME J. Fluids Eng., **125**, pp. 500–509.

[6] Krajnović, S., and Davidson, L., 2005, "Flow Around a Simplified Car, Part 1: Large Eddy Simulation," ASME J. Fluids Eng., **127**, pp. 907–918.

[7] Jeong, J., and Hussain, F., 1995, "On the Identification of a Vortex," J. Fluid Mech., **285**, pp. 69–94.

[8] Sujudi, D., and Haimes, R., 1995, "Identification of Swirling Flow in 3-D Vector Fields," AIAA Pap., paper no. AIAA 95-1715.

[9] Computational Engineering International, Ins., Apex, USA, 2003, *EnSight User Manual for Version 7.6*.

[10] Perry, A. E., and Chong, M. S., 1987, "A Description of Eddying Motions and Flow Patterns Using Critical-Point Concepts," Annu. Rev. Fluid Mech., **19**, pp. 125–155.

[11] Krajnović, S., and Davidson, L., 2002, "Exploring the Flow Around a Simplified Bus with Large Eddy Simulation and Topological Tools," in *The Aerodynamics of Heavy Vehicles: Trucks, Busses and Trains* (Spinger, Monterey, CA).